Relativistic effects on the collisionless–collisional transition of the filamentation instability in fast ignition

M. F I O R E, F. F I Ú Z A, M. M A R T I, R. A. F O N S E C A†
and L. O. S I L V A

GoLP/Instituto de Plasmas e Fusão Nuclear – Laboratório Associado,
Instituto Superior Técnico, 1049-001 Lisboa, Portugal
(luis.silva@ist.utl.pt)

Abstract. Relativistic collisional effects on the filamentation instability are analytically and numerically investigated by comparing collisionless and collisional scenarios for a fast ignition (FI) configuration. The theoretical kinetic model, including warm species and space charge effects, predicts the preferential formation of larger filaments and the inhibition/enhancement of the instability when collisions are accounted for. These collisional effects are qualitatively and quantitatively confirmed by 1D and 2D particle-in-cell (PIC) simulations, also providing a physical picture for the inhibition/enhancement regime due to collisions, based on the electron beam slowdown. By plugging typical FI parameters in the dispersion relation, the theoretical model predicts significant growth rates of the instability deep inside the FI target, thus showing the potential role of the filamentation instability as a mechanism for energy deposition into the pellet core.

---

1. Introduction

Since the seminal work of Tabak et al. [1], the fast ignition (FI) approach to thermonuclear fusion by inertial confinement has received an immediate and increasing interest, also due to very promising experimental results [2]. Many efforts have been devoted to numerically simulate the PW-laser pulse-driven electron beam generation as well as the beam propagation through the steep density gradient inside the compressed fuel pellet and the energy deposition into the core. The advance in understanding and controlling the complex physics involved in these three crucial stages allowed by numerical codes has been accompanied by an intense theoretical activity, in which one of the most extensively explored subjects of the last years has been the collisionless Weibel-like filamentation instability [3].

Also invoked in astrophysics as a mechanism to generate the intense magnetic fields in gamma-ray bursts (GRBs) [4], the filamentation instability can show up in the coronal region of the FI fuel target, when the MA-current carried by the MeV-beam electrons is compensated by a return current as a natural response of the background plasma [5]. As a consequence of the Lorentz force due to a magnetic field fluctuation being amplified by the filamentation instability, beam and plasma

† Also at DCTI, ISCTE – Lisbon University Institute, Portugal.

particle trajectories undergo a deflection, which is responsible for the current filament formation. After the linear stage of the instability, filaments start to merge. This non-linear dissipative process can be either deleterious if it occurs in the coronal region by preventing the beam propagation, or useful by depositing the beam energy into the pellet core. Linear treatment allows to calculate the growth rate (Γ) of the linear stage of the collisionless filamentation instability, thus providing theoretical predictions about the occurrence and the evolution of the instability, filament size and the maximum value B_{sat} of the magnetic field generated at saturation, because $B_{sat} \propto \Gamma^2$ [6].

Moving from the corona toward the center of the pellet, the very high particle densities in inner regions of the compressed FI target make the collision frequency v significant in comparison with the electron plasma frequency ω_{pe}. Therefore, collisions have to be included in any numerical or analytical study in order to properly examine the roles of the filamentation instability in inner zones of the FI target.

Implicit particle-in-cell (PIC) simulations [7], including the effects of electron Rutherford scattering, demonstrated the suppression of the Weibel instability by collisions. However, a non-relativistic analytical study [8] showed that the collisional filamentation instability always occurs, regardless of the transverse temperature: For temperatures at which the collisionless instability is suppressed, collisions guarantee a small but non-negligible growth rate. This counterintuitive effect of the instability enhancement, when collisions are accounted for, was also found in more recent works by employing fluid [9] and kinetic theories [10]; nevertheless this aspect has not been studied in detail yet and no physical picture explaining this effect was put forward. Only recently, a non-relativistic theoretical analysis [11] showing the inhibition/enhancement of the collisional filamentation instability provided a physical picture of this phenomenon: whereas collisions lead to a detuning between particle perturbations and their corresponding reactive fields, thus decreasing the growth rate in a symmetric counterstreaming configuration, collisional effects can also decrease this stabilization effect in an asymmetric counterstreaming scenario, leading to an enhancement of the instability. A relativistic analysis followed [12], not including space-charge effects, where similar results were observed. These studies are either limited to the non-relativistic case or do not include space-charge effects. A complete relativistic analysis, including space charge effects and a numerical study, to compare the theoretical predictions is missing. The opposite conclusions of a suppression or an enhancement of the filamentation instability due to collisions show the need to clarify, both theoretically and numerically, how the collisionless–collisional transition affects the instability, what are the relativistic effects on the transition and what is the general role of collisions in these scenarios.

In this paper, the linear stage of the collisional filamentation instability is theoretically and numerically analyzed for a FI configuration involving an electron beam, a corresponding electron return current and a background of cold ions, employing relativistic kinetic theory and PIC simulations with relativistic binary collisions. Collisions are analytically included through the particle-number-conserving Krook model [13] and space charge effects are considered, in order to account for first order longitudinal modes coming from the charge imbalance due to the different rate at which species filament [14, 15] (Sec. 2). In Sec. 3, a detailed growth rate analysis by varying the collision frequency, as well as the transverse temperature of
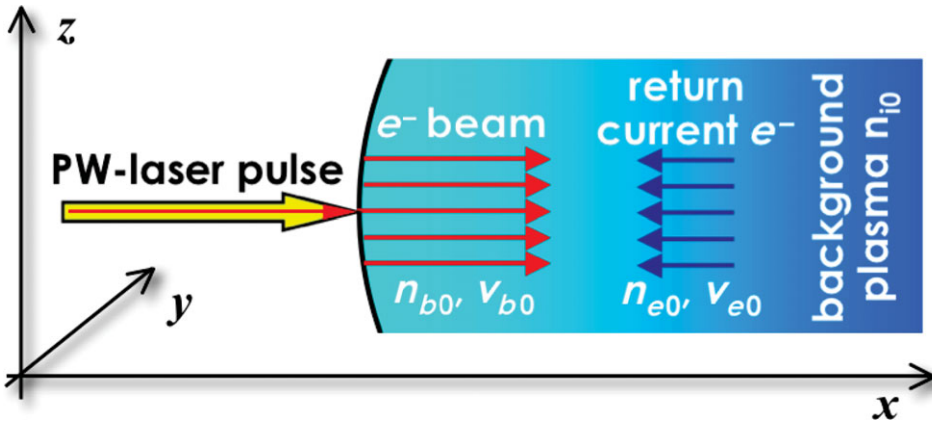
Figure 1. (Colour online) Scheme of the simplified scenario for the theoretical model.

the species, shows two main effects due to collisions: (i) the preferential formation of larger filaments than those in collisionless regime and (ii) collisions can lead to either an inhibition or an enhancement of the filamentation instability.

Hybrid codes, in which fast electrons are treated as particles and background electrons as a cold stationary fluid [16], are very useful to perform multi-dimensional simulations of FI scenarios, not yet possible with PIC codes because of computational limitations. However, hybrid codes pay the price of the loss of spatial and temporal resolution at the scales of the kinetic effects mentioned above, for which the electron collisionless skin depth c/ω_{pe} and the electron plasma period ω_{pe}^{-1} must be resolved. In order to properly study these kinetic effects, PIC codes with collisions are required.

PIC simulations with relativistic binary collisions are presented in Sec. 4: based on both numerical and theoretical considerations, a physical picture to explain the enhancement/inhibition regime due to collisions is illustrated, deriving from relativistic effects and electron beam slowdown; furthermore, a direct comparison between theoretical and numerical growth rates of the filamentation instability is presented. In Sec. 5, a parametric study of FI typical scenarios shows that, according to the theory, the filamentation instability can occur deep inside the FI target, thus making the instability a mechanism that may contribute to energy deposition into the core. Finally, the main conclusions are summarized in Sec. 6.

2. Theoretical model

In order to model the interaction between electron beam and plasma return current inside the PW-laser hit FI target, we consider a simplified scenario according to Fig. 1, where beam electrons and return current plasma electrons move along one direction without any divergence. Plasma ions are the neutralizing background and are assumed cold.

To perform our theoretical analysis of the collisional filamentation instability, we employ relativistic kinetic theory, choosing the particle-number-conserving Bhatnagar–Gross–Krook (BGK or Krook) model [13,18] for the collision term. Although only a Fokker–Planck collisional operator guarantees both particle-number

and energy conservation, the advantage of the particle-number-conserving BGK model resides in its relative simplicity to carry out analytical calculations. Furthermore, a numerical assessment of the Krook operator [19] has shown the accuracy of the particle-number-conserving version of the BGK model when compared with both particle-number and energy-conserving models. Another important result of that study is the inadequacy of the simpler and often used non-conserving Krook operator, where the replacement of the frequency ω by $\omega + iv$ is the only change to be made in the collisionless dispersion relation when collisions are accounted for. Therefore, the choice of the particle-number-conserving Krook model is a good trade-off between accuracy and analytical simplicity, keeping in mind that it is valid as long as the collision frequency, in general a function of velocity, can be considered constant (e.g. electron–ion collisions). The perturbed relativistic Maxwell–Boltzmann equation reads

$$\frac{\partial f_{1s}}{\partial t} + \mathbf{v}_{0s} \cdot \nabla f_{1s} + q_s \left(\mathbf{E}_1 + \frac{\mathbf{v}_{0s}}{c} \times \mathbf{B}_1 \right) \cdot \nabla_{\mathbf{p}} f_{0s} = \underbrace{-v_s (f_{1s} - n_{1s} F_{0s})}_{\mathscr{K}}, \qquad (1)$$

where the species s is described by the perturbed (f_1) and the unperturbed ($F_0 = f_0/n_0$) distribution function, the charge q, the mass m, the unperturbed velocity $\mathbf{v}_0$, the perturbed density $n_1 = \int f_1(\mathbf{p}) d\mathbf{p}$ and the collision frequency v; $\mathscr{K}$ is the collision term provided by the Krook model and is also called the Krook operator. As for the study of the Weibel instability in the dynamics of collisionless counter-streaming plasma shells in GRB scenarios [15], we take the space charge effects into account by keeping the component of the electric field $\mathbf{E}$ along the wave vector $\mathbf{k}$ in our calculations. Thus, the filamentation instability examined here is not purely electromagnetic (i.e. $\mathbf{k} \cdot \mathbf{E} \neq 0$) due to the different pinching rate of electrons and ions leading to a charge imbalance and a consequent longitudinal electric field established in the region surrounding each filament [14]. We choose a waterbag distribution function

$$F_{0s} = \frac{1}{2p_{z0,s}} \delta(p_x - p_{x0,s}) \delta(p_y) [\Theta(p_z + p_{z0,s}) - \Theta(p_z - p_{z0,s})], \qquad (2)$$

in which p_{x0} is the momentum in the x direction, p_{z0} is the momentum thermal spread in the z direction and $\Theta(x)$ is the Heaviside step function. For our choice, the distribution function F_{0s} describes a cold species s in the x and y directions, propagating along the x direction, with a thermal spread along the z direction, which defines the transverse direction. As return current plasma electrons have the largest collision frequency v_e, for the sake of simplicity only collisions made by them are considered in the calculations [20]. Following the same technique outlined in [15] and considering perturbations $\propto \exp[i(\omega t - kz)]$, the perturbed plasma electron distribution function is

$$f_{1e} = -\frac{i}{\omega - kv_{ze}} \frac{en_{0e}}{\omega} \{ [(\omega - kv_{ze})\partial_{p_x} + kv_{xe}\partial_{p_z}] F_{0e} E_x$$

$$+ [(\omega - kv_{ze})\partial_{p_y} + kv_{ye}\partial_{p_z}] F_{0e} E_y + \omega \partial_{p_z} F_{0e} E_z \} + \frac{iv_e}{\omega + iv_e - kv_{ze}} F_{0e} n_{1e}. \qquad (3)$$

As $n_{1e} = \int f_{1e}(\mathbf{p}) d\mathbf{p}$ (the subscript "e" refers to plasma electrons), after performing the integration and assuming that $p_{x0,e} \gg p_{z0,e}$ (i.e. $\gamma_e \approx [1 + p_{x0,e}^2/(m_e^2 c^2)]^{1/2}$), the

perturbed electron plasma density is

$$n_{1e} = -\frac{ien_{0e}}{\omega^2} \int d\mathbf{p} \frac{\Upsilon_{xz}F_{0e}E_x + \Upsilon_{yz}F_{0e}E_y + \partial_{p_z}F_{0e}E_z}{\omega^\dagger - kv_z} \left(1 - \frac{iv_e}{2kc\beta_{th0,e}}L\right)^{-1}, \quad (4)$$

where $\beta_{th0,e}$ stands for the plasma electron thermal velocity and with the definitions $\omega^\dagger = \omega + iv_e$, $\Upsilon_{mn} = [(1 - kv_z/\omega)\partial_{p_m} + (kv_m/\omega)\partial_{p_n}]$ and $L = \ln[(\omega^\dagger + kc\beta_{th0,e})/(\omega^\dagger - kc\beta_{th0,e})]$.

Inserting (4) in (1), the dispersion relation for waves propagating in the z direction with wave vector $\mathbf{k} = k\mathbf{e}_z$ is obtained by combining (1) and Faraday's and Ampère's equations yielding [17]

$$(\omega^2 - k^2c^2 + C_{xxz})[(\omega^2 - k^2c^2 + C_{yyz})(\omega^2 + D_z) - D_y C_{zyz}] - C_{xyz}[C_{yxz}(\omega^2 + D_z)$$

$$- D_y C_{zxz}] + D_x[C_{yxz}C_{zyz} - (\omega^2 - k^2c^2 + C_{yyz})C_{zxz}] = 0, \quad (5)$$

where the coefficients in (5) are given by summing up the contributions of the three species, calculated with

$$\begin{pmatrix} C_{lmn,s} \\ D_{l,s} \end{pmatrix} = \omega_{p0,s}^2 m_s \int d\mathbf{p} \left\{ \frac{\omega v_l}{\omega^\dagger - kv_z} \begin{pmatrix} \Upsilon_{mn} \\ \partial_{p_z} \end{pmatrix} F_{0s} \right\} \quad (6)$$

for the collisionless species, namely beam electrons ("b") and cold plasma ions ('i'), and the contribution of plasma electrons is

$$\begin{pmatrix} C_{lmn,e} \\ D_{l,e} \end{pmatrix} = \omega_{p0,e}^2 m_e \int d\mathbf{p} \left\{ \frac{\omega v_l}{\omega^\dagger - kv_z} \begin{pmatrix} \Upsilon_{mn} \\ \partial_{p_z} \end{pmatrix} F_{0e} \right.$$

$$\left. - iv_e \frac{\omega v_l}{\omega^\dagger - kv_z} \frac{F_{0e}}{1 - (iv_e/2kc\beta_{th0,e})L} \int d\mathbf{p} \frac{1}{\omega^\dagger - kv_z} \begin{pmatrix} \Upsilon_{mn} \\ \partial_{p_z} \end{pmatrix} F_{0e} \right\}, \quad (7)$$

where $\omega_{p0,s}$ stands for the plasma frequency of the species s. Hence $C_{lmn} = \sum_s C_{lmn,s}$ and $D_l = \sum_s D_{l,s}$. It is worth pointing out that whereas the equivalent coefficients of the dispersion relation for the collisionless filamentation instability admit any distribution function [15], in the coefficients (7) the choice of the distribution function has been already made, being necessary to calculate the perturbed density n_1 through (4) appearing in the Krook operator. A waterbag distribution function allows to deal with relativistic kinetic calculations in a closely analytical form, concerning the p_m-, p_n- and p_z-integrations involved in the coefficients (6) and (7). Furthermore, Cottrill et al. [20] have shown that the relativistic waterbag distribution guarantees reasonable approximations to instability growth, even with collisions. After performing the integration over the distribution function (note that $C_{xyz} = C_{yxz} = C_{zyz} = D_y = 0$), the dispersion relation is reduced to

$$(\omega^2 - k^2 + [C_{xxz}])(\omega^2 + [D_z]) - [C_{zxz}][D_x] = 0, \quad (8)$$

where the coefficients in square brackets are normalized in time to the electron plasma period $1/\omega_{p0,e}$ and in space to the electron plasma skin depth $c/\omega_{p0,e}$ yielding (from

now on, the subscript '0' indicating zeroth-order quantities is omitted)

$$[C_{xxz}] = -\left\{ \mathscr{F} + \sum_s \left[\frac{n_s}{m_s}\right] \frac{1}{\gamma_s} \frac{k^2\beta_s^2}{\omega^2 - k^2\beta_{th,s}^2} + \left[\frac{n_e}{m_e}\right] \left[\frac{\beta_e^2}{\gamma_e} \frac{iv_e\omega^\dagger + k^2}{\omega^{\dagger 2} - k^2\beta_{th,e}^2} - \frac{iv_e L}{2u_{th,e}k} \right. \right.$$

$$\left. \left. - \frac{iv_e\beta_e^2 L}{[1 - (iv_e L/2\beta_{th,e}k)]2u_{th,e}k} \left(\frac{iv_e L}{2\beta_{th,e}k} - \frac{iv_e\omega^\dagger + k^2}{\omega^{\dagger 2} - k^2\beta_{th,e}^2} \right) \right] \right\} \tag{9a}$$

$$[D_z] = -\left\{ \sum_s \left[\frac{n_s}{m_s}\right] \frac{1}{\gamma_s} \frac{1}{\omega^2 - k^2\beta_{th,s}^2} \omega^2 \right.$$

$$\left. + \left[\left[\frac{n_e}{m_e}\right] \frac{1}{\gamma_e} \frac{\omega}{\omega^{\dagger 2} - k^2\beta_{th,e}^2} \left[\omega^\dagger - \frac{iv_e}{[1 - (iv_e L/2\beta_{th,e}k)]} \left(1 - \frac{\omega^\dagger L}{2\beta_{th,e}k} \right) \right] \right] \right\} \tag{9b}$$

$$[C_{zxz}] = -\left\{ \sum_s \left[\frac{n_s}{m_s}\right] \frac{1}{\gamma_s} \frac{k\beta_s}{\omega^2 - k^2\beta_{th,s}^2} \omega + \left[\frac{n_e}{m_e}\right] \left[\frac{\omega^\dagger\beta_e}{\gamma_e k} \left(\frac{iv_e\omega^\dagger + k^2}{\omega^{\dagger 2} - k^2\beta_{th,e}^2} - \frac{iv_e L}{2\beta_{th,e}k} \right) \right. \right.$$

$$\left. \left. + \frac{iv_e\beta_e(2k\beta_{th,e} - \omega^\dagger L)}{[1 - (iv_e L/2\beta_{th,e}k)]2u_{th,e}k^2} \left(\frac{iv_e L}{2\beta_{th,e}k} - \frac{iv_e\omega^\dagger + k^2}{\omega^{\dagger 2} - k^2\beta_{th,e}^2} \right) \right] \right\} \tag{9c}$$

$$[D_x] = -\left\{ \sum_s \left[\frac{n_s}{m_s}\right] \frac{1}{\gamma_s} \frac{k\beta_s}{\omega^2 - k^2\beta_{th,s}^2} + \left[\frac{n_e}{m_e}\right] \left[\frac{1}{\gamma_e} \frac{k\beta_e}{\omega^{\dagger 2} - k^2\beta_{th,e}^2} \right. \right.$$

$$\left. \left. + \frac{iv_e L}{[1 - (iv_e L/2\beta_{th,e}k)]2u_{th,e}} \frac{\beta_e}{\omega^{\dagger 2} - k^2\beta_{th,e}^2} \right] \right\} \omega, \tag{9d}$$

where the sum in j is over beam electrons and ions, and n is normalized to the background density, m is normalized to the electron mass, β is the velocity along the x direction and β_{th} is the perpendicular thermal velocity, with the standard definitions $\gamma = (1 - \beta^2 - \beta_{th}^2)^{-1/2}$, $u = \gamma\beta$ and $u_{th} = \gamma\beta_{th}$, complemented by the definition

$$\left(\overline{\frac{1}{\gamma_s}} \right) = \int d\mathbf{p} \frac{F_s}{\gamma} = \frac{1}{2u_{th,s}} \ln \left(\frac{1 + \beta_{th,s}}{1 - \beta_{th,s}} \right) \tag{10}$$

for our choice of the distribution function (2), where 's' is for each one of the three species considered, and with

$$\mathscr{F} = \sum_{s=1}^3 \left[\frac{n_s}{m_s}\right] \left[\left(\overline{\frac{1}{\gamma_s}} \right) - \frac{1}{\gamma_s} \frac{u_s^2}{1 + u_s^2} \right]. \tag{11}$$

After solving the dispersion relation for the perturbation frequency ω, it is possible to evaluate the growth rate of the instability that corresponds to the largest positive imaginary part of ω. Due to its complexity, the dispersion relation will be solved numerically.
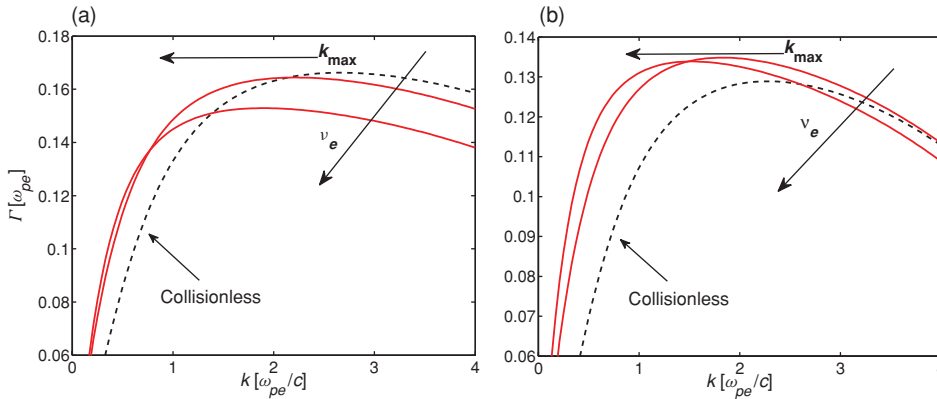
Figure 2. (Colour online) Shifting of k_{max} toward smaller ks. Growth rate of the collisionless (black dashed line) and collisional (red solid line) filamentation instability versus wavenumber for $T_{\perp b} = 0.13$ keV, $T_{\perp e} = 10$ eV and $\alpha = 0.1$, for an electron collision frequency $v_e = 0.25, 0.75$: (a) for $u_b = 0.83$, collisions lead to an inhibition of the instability, (b) for $u_b = 5$, collisions lead to an enhancement.

3. Collisional effects on the filamentation instability

To examine collisional effects on the growth rate of the filamentation instability predicted by the theory, we first choose a relativistic electron beam characterized by $u_b = \gamma_b \beta_b = 0.83$ and a thermal velocity $\beta_{th,b} = 0.024$, which corresponds to a transverse temperature $T_{\perp b} = 0.13$ keV according to the expression, for a species s, obtained from the energy–momentum tensor $T_{\perp s} = \int d\mathbf{p}\, p_z v_z F_s$, yielding

$$\frac{k_B T_{\perp s}}{m_s c^2} = \frac{\gamma_s}{2} \left[1 + \frac{1 - \beta_{th,s}^2}{2\beta_{th,s}} \ln \left(\frac{1 - \beta_{th,s}}{1 + \beta_{th,s}} \right) \right] \tag{12}$$

for a relativistic waterbag distribution function [21]. Being the ratio $\alpha = n_b/n_i$ between the beam electron density n_b and the plasma ion density n_i, charge conservation is guaranteed by imposing $n_e = (1 - \alpha)n_i$. Current is also conserved, establishing a constraint on the return current electron velocity $\boldsymbol{\beta}_e = \frac{\alpha}{1-\alpha}\boldsymbol{\beta}_b$, where $\boldsymbol{\beta}_b = -\beta_b \mathbf{e}_x$ is the beam electron velocity. Ions are initialized as cold and stationary, but are free to move as the instability grows.

In Fig. 2(a), the growth rate Γ of the filamentation instability is plotted for all wavenumbers, comparing the collisionless case with collisional scenarios with normalized electron collision frequencies $v_e = 0.25$ and 0.75, for $\alpha = 0.1$ and a transverse temperature of the return current electrons $T_{\perp e} = 10$ eV. As v_e increases, the wavenumber k_{max} corresponding to the maximum growth rate Γ_{max}, is shifted toward smaller ks, i.e. larger wavelengths. This shifting due to collisions indicates a preferential formation of larger filaments than those formed in collisionless scenarios. Another effect shown in Fig. 2(a), by comparing the collisionless and collisional growth rate, is that even though collisions increase Γ for small modes, Γ_{max} is decreased and the filamentation instability is weakened for high modes [22]. However, by changing $u_b = 5$ and consequently the beam electron transverse temperature $T_{\perp b} = 0.5$ keV according to (12), the growth rate of the collisional filamentation instability is larger than in the collisionless case for a wider range of wavenumbers,
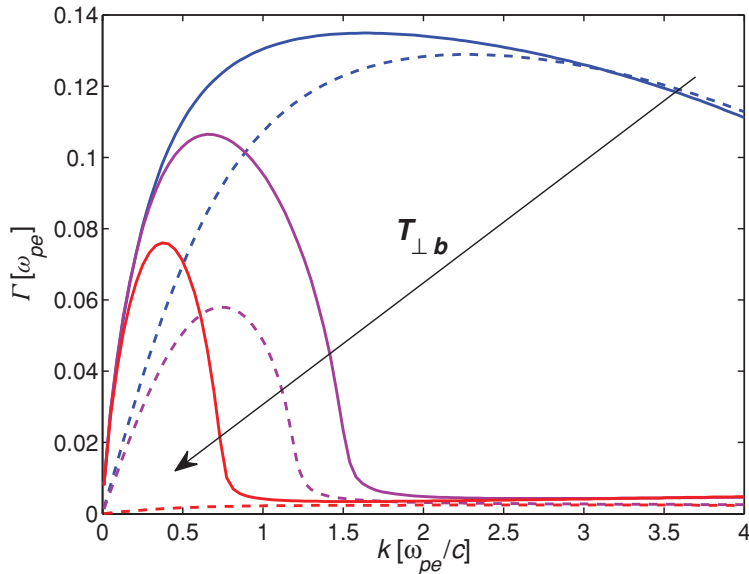
Figure 3. (Colour online) Enhancement of the filamentation instability due to collisions. Growth rate as a function of wavenumber in collisionless (dashed lines) and collisional (solid lines) scenarios for $u_b = 5$, $T_{\perp e} = 10$ eV, $\alpha = 0.1$, a fixed $v_e = 0.5$ and increasing beam electron transverse temperature: $T_{\perp b} = 0.5$ keV (blue lines), $T_{\perp b} = 9$ keV (magenta lines) and $T_{\perp b} = 34$ keV (red lines).

as shown in Fig. 2(b). Furthermore, $\Gamma_{\max}$ is larger when collisions are included, the shifting of $k_{\max}$ toward larger λ's being always present.

The growth rate of the filamentation instability for a proper velocity of the beam electrons $u_b = 5$, plasma electron transverse temperature $T_{\perp e} = 10$ eV and beam electron and ion density ratio $\alpha = 0.1$, for increasing $T_{\perp b}$, is depicted in Fig. 3, comparing collisionless and collisional cases; $v_e = 0.5$ is kept fixed for collisional Γ's. Although the instability is weakened by transverse thermal effects, the maximum value of the growth rate of the filamentation instability when collisions are accounted for is always larger than in the collisionless scenarios, and the enhancement is predicted for a wide range of unstable modes, becoming stronger for large transverse temperature. At $T_{\perp b} = 34$ keV, the occurrence of the filamentation instability is guaranteed by collisions, whereas only moving ions allow for the tiny growth rate appearing in Fig. 3: the collisionless filamentation instability would be completely shut down otherwise [15]. Therefore, according to the theory, collisions guarantee the occurrence of the filamentation instability regardless of the transverse temperature [8].

The $k_{\max}$ shifting toward small wavenumbers also occurs in collisionless scenarios because of large transverse temperatures, as shown in Fig. 3. Collisions have a similar effect as the thermal pressure force, which prevents the formation of small filaments by acting against the magnetic pinching force. The shifting of $k_{\max}$ is dominated by collisions as long as the transverse temperature is relatively small. As $T_{\perp b}$ increases, the effect of thermal pressure takes over and scenarios exist in which the collisionless $k_{\max}$ is smaller than the collisional one.
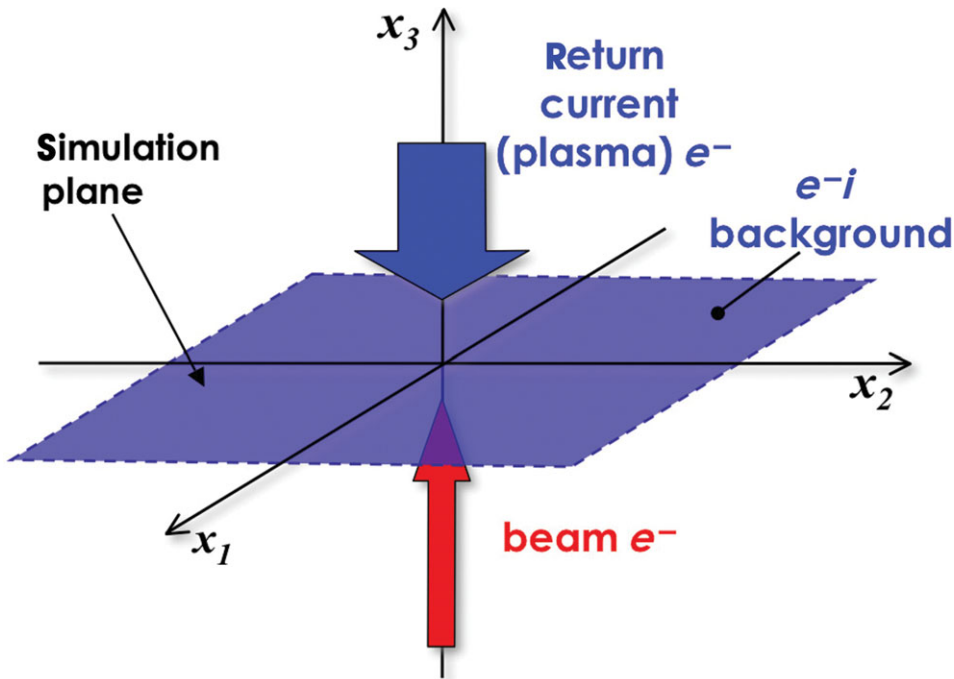
Figure 4. (Colour online) Set-up of simulations for the numerical study of collisional effects on the filamentation instability.

As the filamentation instability is fed by the kinetic energy of the electron beam, and the Weibel instability is fed by the temperature anisotropy of a species [7], collisions should always lead to an inhibition of the instability through isotropization. The counterintuitive result of the enhancement of the filamentation instability due to collisions, predicted by the theory, suggests that other kinetic effects may play more important roles than isotropization. Since finding an explicit expression for Γ from the dispersion relation (8) is not possible analytically, this intriguing issue will be addressed in the next section by resorting to PIC simulations.

4. PIC simulations of the collisional filamentation instability

As shown in Fig. 4, the chosen set-up for PIC simulations is represented by a 2D perpendicular configuration with the counter-streaming beam electrons and the return current electrons (from the background) propagating along the x_3 direction perpendicular to the x_1–x_2 simulation plane; ions represent the neutralizing background. Simulations are carried out with the PIC code OSIRIS 2.0 [23]; relativistic collisions are included through a binary collision model [24] based on an extension of the non-relativistic Monte-Carlo method proposed by Takizuka and Abe [25]. Simulations are performed on a 640×640 grid, with 64×4 particles-per-cell (ppc) per species and three species, thus leading to a total of 315 million particles. The distribution of the particles in a cell is motivated by the fact of having more resolution in the hot x_1 direction, along which the density is initially perturbed by the filamentation instability. Temporal and spatial scales in the simulations are

normalized to the inverse electron plasma frequency ω_{pe}^{-1} and the collisionless skin depth $\lambda_e = c/\omega_{pe}$, respectively; charges and masses are measured in the units of the electron charge e and the electron mass m_e. In these normalized units and by choosing a grid cell size $\Delta x_1 = \Delta x_2 = 0.1\ c/\omega_{pe}$, the box size is $64.0 \times 64.0\ (c/\omega_{pe})^2$ and the time step is $\Delta t = 0.07\ \omega_{pe}^{-1}$. The simulation duration for both collisionless and collisional scenarios is $70.0\ \omega_{pe}^{-1}$ in order to analyze the linear phase of the instability. Periodic boundary conditions are used. The initial fluid momentum of beam electrons, along the x_3 direction, is $u_b = \gamma_b \beta_b = 5$, whereas the fluid momentum of the return current (plasma) electrons is obtained by imposing current neutrality, considering a beam electron–ion density ratio $\alpha = 0.1$. Beam and plasma electrons have a thermal spread with the root-mean-square momentum (rms) $u_{th} = \gamma_0 \beta_{th}$ of $u_{th,b} = 0.122$ and $u_{th,e} = 0.0077$, respectively, along the transverse x_1 direction, with a waterbag distribution function. For collisional simulations, extra parameters have to be specified as inputs. We consider a numerical collision of the particles for each time step, collision cells having the size of 20×20 PIC cells and a fixed Coulomb logarithm to speed up the simulations. To reduce the numerical noise and to save computational time, only plasma electron–ion collisions are included; simulations with all species making collisions were performed, and no crucial differences were observed. In order to observe collisional effects earlier in time, we use a large collision frequency $v_{ei} = 0.57\ \omega_{pe}$ calculated with the general formula (in SI units) for colliding species 'α' and 'β'

$$v_{\alpha\beta} = \frac{\ln \Lambda_{\alpha\beta}}{4\pi} \left(\frac{q_\alpha q_\beta}{\varepsilon_0 \mu_{\alpha\beta}} \right)^2 \frac{n_\beta\ g_{\alpha\beta}^{-3}}{\gamma_{\alpha\beta}^2}, \tag{13}$$

where q_α and q_β represent the charges of the species, ε_0 is the permittivity of free space, $\mu_{\alpha\beta}$ is the reduced mass, n_β is the number density, $g_{\alpha\beta}(=|\mathbf{v}_\alpha - \mathbf{v}_\beta|)$ and $\gamma_{\alpha\beta}$ are the relative velocity and the corresponding Lorentz factor, respectively, and $\ln \Lambda_{\alpha\beta}$ is the Coulomb logarithm.

The comparison between the collisionless and collisional dynamics of the beam electron density is shown in Fig. 5 for three different times progressively. The initially uniform electron beam breaks up in filaments as the filamentation instability occurs; after being formed, filaments start to merge as shown in the last frame of the figure. By comparing the two scenarios, it is evident that the size of the filaments in the collisional regime is larger than the size in the collisionless regime. The theoretical prediction of the shifting of the wavenumber $k_{\max}$ corresponding to the maximum growth rate of the filamentation instability toward smaller wavenumbers, i.e. larger wavelengths, is confirmed by the simulations. Collisions lead to a preferential formation of larger filaments than those in collisionless scenarios.

Further collisional effects can be evidenced by examining the temporal evolution of the fluid momentum in the propagation direction p_3 ($p_i = u_i$ in simulation units, for $i = 1, 2, 3$) as a function of the momentum in the transverse hot direction p_1. As for the p_3–p_1 evolution for plasma electrons, from Fig. 6 we can observe that, within the linear stage of the collisionless filamentation instability, there is no change of momenta. Only in the last frame at $50.4\ \omega_{pe}^{-1}$, where the instability is about to enter the nonlinear stage, the slight increase of the p_1 spread indicates plasma electron heating. The same simulation, with the inclusion of collisions, shows a completely different plasma electron behavior. As soon as the simulation begins,
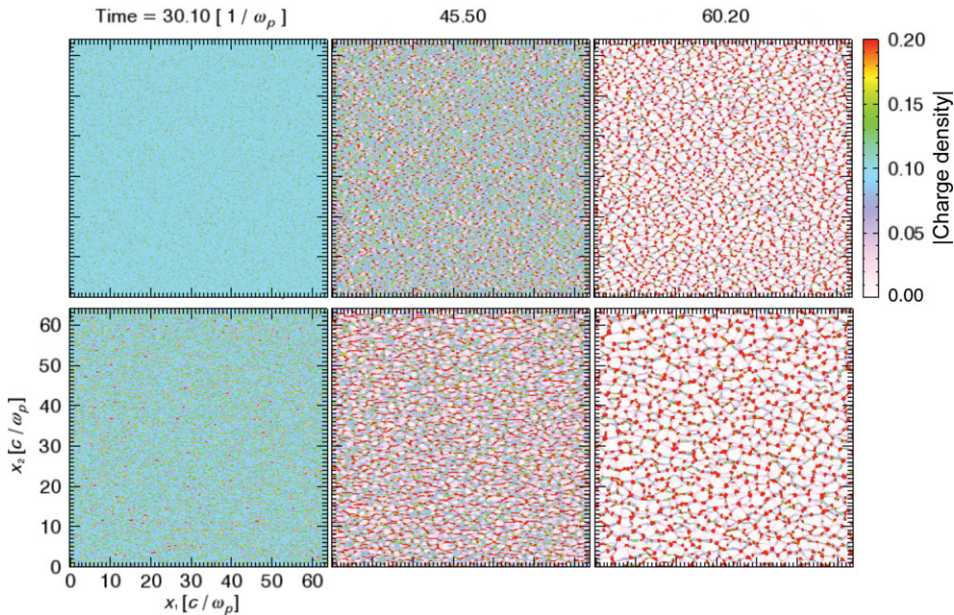
Figure 5. (Colour online) Temporal evolution of the beam electron density: collisionless simulation in the upper row, collisional simulation in the lower row. The preferential formation of larger filaments when collisions are included confirms the theoretical prediction of the k_{max} shifting toward large wavelengths.
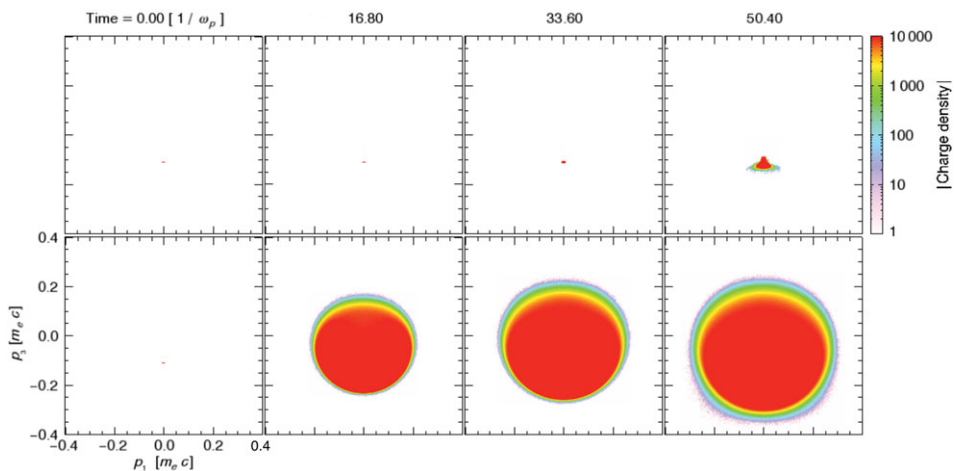

Figure 6. (Colour online) Temporal evolution of the propagation and transverse momenta of the plasma electrons: collisionless simulation in the upper row, collisional simulation in the lower row. The strong isotropization due to collisions is evident.

a strong isotropization due to collisions is observed, characterized by almost the same momentum spread in both directions during the entire linear stage of the filamentation instability, represented by a circle in the p_3–p_1 plot. The collisionless p_3–p_1 temporal evolution of beam electrons shows the same features of plasma
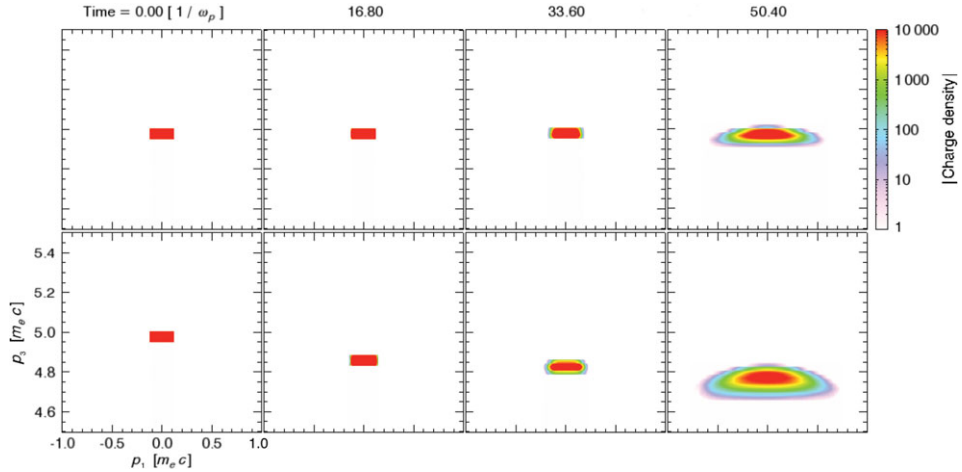
Figure 7. (Colour online) Temporal evolution of the propagation and transverse momenta of the beam electrons: collisionless simulation in the upper row, collisional simulation in the lower row. The most important observed effect is the beam slowdown due to collisions.

electrons, with the initial distribution unchanged during the linear phase of the instability and a slight heating as the filamentation instability enters the nonlinear stage (see Fig. 7). When collisions are included in the simulations, beam electrons undergo a progressive slowdown during the entire linear phase of the instability. At $50.4\,\omega_{pe}^{-1}$, beam electrons heat up slightly more than in the collisionless scenario, but within the linear phase of the instability there is, interestingly, almost no changes in the transverse momentum.

As observed, when the collision frequency is high enough (i.e. $v_{ei}/\omega_{pe} \sim 0.1-1$), the beam slows down before the instability develops. Thus, it is instructive to understand how the beam electron slowdown affects the growth rate of the filamentation instability. To do that, and as we are assuming that the only role of collisions is to slow down the beam, the collisionless relativistic fluid theory can be employed. For a simplified scenario with two counter-streaming beams with the same density, the growth rate of the filamentation instability reads

$$\Gamma \propto \beta_b \sqrt{\frac{\alpha}{\gamma_b}}. \tag{14}$$

In Fig. 8, the growth rate, shown in (14), of the filamentation instability is plotted as a function of γ_b for the contrast ratio we used in the simulations $\alpha = 0.1$. Due to a high collisionality, beam electrons first slow down, then they lead to a filamentation where the actual γ_b is lower than the initial one. This scenario can lead to either a smaller or a larger growth rate [20], depending on the initial value of γ_b. Being $\gamma_{b,\max} \approx 1.73$ the Lorentz factor corresponding to the maximum growth rate, if the initial $\gamma_b \lesssim \gamma_{b,\max}$, the slowdown of the beam electrons due to collisions leads to an inhibition of the filamentation instability. On the other hand, if the initial $\gamma_b \gtrsim \gamma_{b,\max}$, the slowdown of the beam electrons due to collisions leads to an enhancement of the filamentation instability.

According to the theoretical model described in Sec. 2, the Lorentz factors appearing in the coefficients (9a) of the dispersion relation are 0th order quantities,
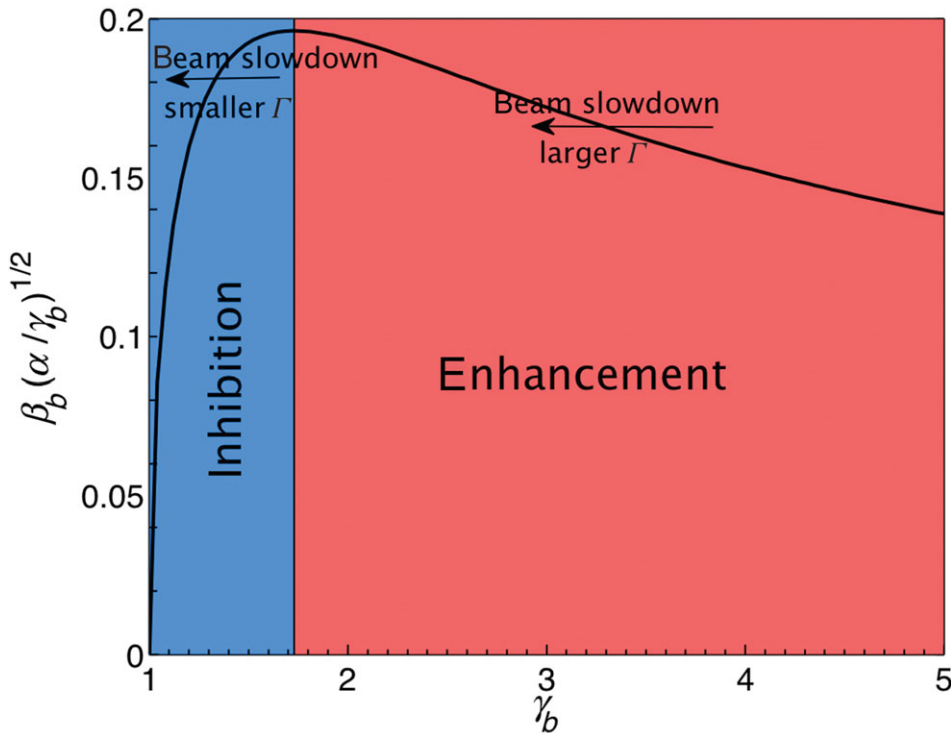
Figure 8. (Colour online) Ratio proportional to the collisionless relativistic fluid growth rate of the filamentation instability as a function of γ_b. The beam electron slowdown due to collisions can lead to either an inhibition or an enhancement of the filamentation instability, depending on the initial value of γ_b.

thus treated as constants. However, as long as $v_{ei} > \Gamma$, the plasma feels the stronger collision effects more than the weaker instability effects mainly through $\Im\left(\omega^{\dagger}\right) = \Im(\omega + i v_{ei}) = \Gamma + v_{ei}$ [11], thus indirectly leading to a first-order perturbation $-\gamma_{1b}$ of the initial beam electron Lorentz factor, which affects the filamentation unstable mode contribution to the distribution function evolution. This perturbation is related to the assumption of the 0th order quasi-neutrality $n_b v_b + n_e v_e = 0$, which leads to the treatment of currents due to collisions as first-order effects. The theoretical model fits the physical picture based on the beam electron slowdown.

In order to quantitatively test the collisional effects on the filamentation instability predicted by our theoretical model, as well as the physical picture illustrated above, it is necessary to compare the theoretical and the numerical growth rates of the instability. One of the main difficulties arising in this comparison is the sensitivity of the growth rate of the filamentation instability to the numerical noise. A simulation set-up similar to the one shown in Fig. 4 is chosen. The simulated direction corresponds to the one along which the species have a thermal spread and the density perturbation grows forming the filaments. The advantage of the 1D simulation is that it is possible to increase both the spatial resolution and the number of ppc with a reasonable computational power: the numerical noise is strongly reduced by choosing a grid cell size $\Delta x_1 = 0.025 \, c/\omega_{pe}$ and 5000 ppc/species.

The 1D simulations are performed on a 204 800 grid, with beam and return current electrons moving along the x_3 direction perpendicular to the simulation direction x_1 and moving ions representing the neutralizing background. The three species lead to a remarkable total of 3.072 billion particles. The box size is 5120.0 c/ω_{pe} and the time step is $\Delta t = 0.0249\ \omega_{pe}^{-1}$. In order to test the physical picture of the inhibition and enhancement regimes, the initial beam electron fluid momentum is $u_b = 0.83$, with $u_{th,b} = 0.0312$, for the inhibition simulation, and $u_b = 0.5$, with $u_{th,b} = 0.122$, for the enhancement simulation; in both simulations the thermal velocity is the same ($\beta_{th,b} = 0.024$). The plasma electron thermal momentum is $u_{th,e} = 0.077$, while the initial fluid momentum is established by current neutrality through the contrast ratio α, which, as well as the plasma electron-ion collision frequency, is the same as in the 2D simulations. A waterbag distribution function is used to initialize the species. The simulation durations are 140.0 ω_{pe}^{-1} for the inhibition regime and 70.0 ω_{pe}^{-1} for the enhancement regime, for both collisionless and collisional scenarios, in order to analyze the linear phase of the instability. For the collisional simulations, numerical particles are set to collide each time step, collisions cells have the size of 20 PIC cells and a fixed Coulomb logarithm is considered to speed up the simulations. Periodic boundary conditions are used. Fields and currents are smoothed through the compensator technique and a second-order interpolation method is employed in the collisionless simulations. With these numerical parameters and according to the empirical model provided by Hockney [26], the normalized numerical collision frequency for plasma electrons is $\nu_{\mathrm{num},e} \approx 1.03 \times 10^{-4}\ \omega_{pe}$. As the plasma electron–ion collisions frequency that we use for our 1D simulations is $\nu_{ei} = 0.57\ \omega_{pe}\ (\gg \nu_{\mathrm{num},e})$, numerical collisional effects are significantly smaller than physical collisional effects.

In Fig. 9 the growth rate of the filamentation instability for both collisionless and collisional scenarios is plotted as a function of wavenumber; solid lines are from the theoretical model and markers are taken from the simulation results. The agreement between theory and simulation is very good in both collisionless and collisional scenarios, even though, as expected, the collisional case shows more numerical noise. The theoretical prediction of the shifting of the wavenumber k_{max}, corresponding to the maximum growth rate toward smaller ks due to collisions, is numerically confirmed (cf. Fig. 5). Having $\gamma_b \approx 1.3$, $\alpha = 0.1$ and according to Fig. 8, the inhibition of the filamentation instability due to collisions is quantitatively and qualitatively confirmed by the simulation. Figure 9(b), corresponding to a scenario of $\gamma_b \approx 5.1$ and $\alpha = 0.1$, completes the physical picture of Fig. 8 by showing the enhancement of the filamentation instability due to collisions not only predicted by the theory but also confirmed by the simulation. Having a very good agreement between theory and simulation, the k_{max} shifting is again recovered numerically. Significant numerical noise reduction in collisional simulations is expected as soon as the higher order interpolation schemes are integrated in the OSIRIS 2.0 collision module.

For beam electron thermal velocities $\beta_{th,b} > 0.05$, the agreement between theory and simulations in terms of the growth rate of the filamentation instability is not as good as shown in Fig. 9 in the collisional case, whereas in the collisionless regime the match remains very good. The mismatch in the collisional case shows the limited accuracy of the Krook operator in analytical dealing with collisions. The theory predicts larger growth rates than the ones calculated from simulations. This result suggests that the particle-number-conserving Krook operator can be unreliable for quantitative predictions at large transverse temperatures: the imaginary part
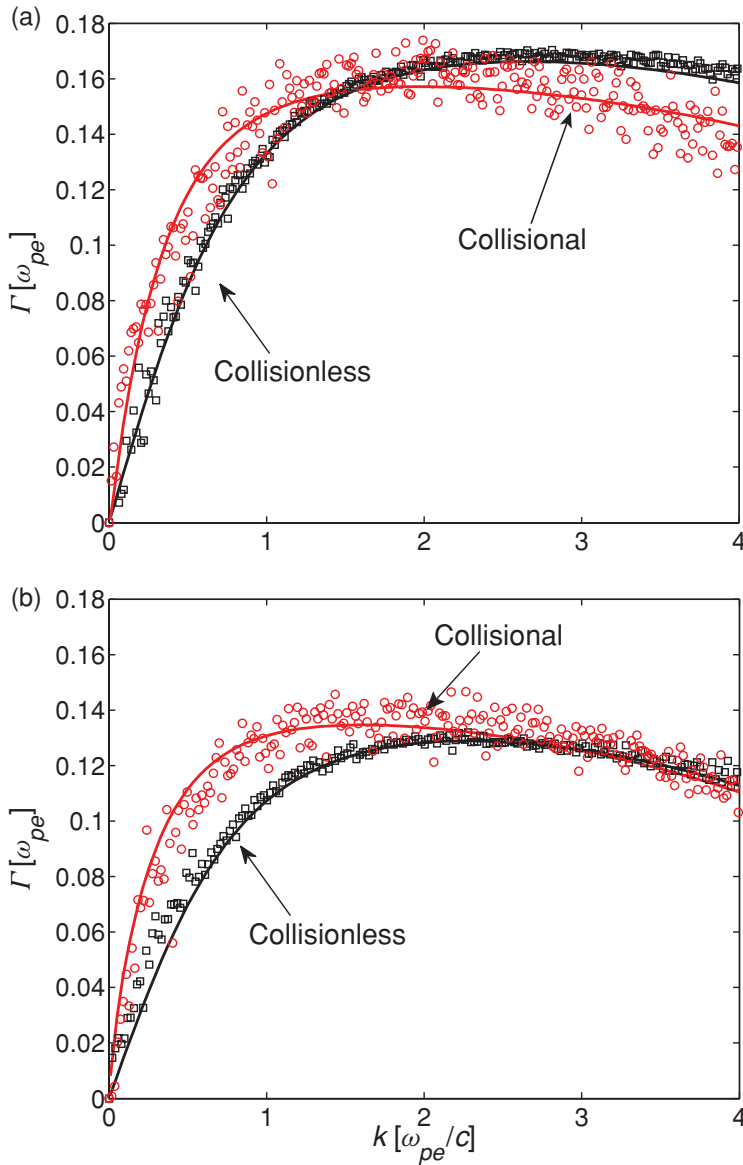
Figure 9. (Colour online) Growth rate of the filamentation instability as a function of wavenumber for $\alpha = 0.1$ and $v_{ei} = 0.57$: comparison between theory (solid lines) and simulations (markers) for (a) $u_b = 0.83$ ($\gamma_b \approx 1.3$) and (b) $u_b = 5$ ($\gamma_b \approx 5.1$). Numerical results quantitatively confirm the k_{max} shifting and the inhibition regime due to collisions predicted by the theory.

of a general dispersion relation (in this case, the growth rate of the collisional filamentation instability) is usually overestimated in comparison with the predictions of a more reliable both energy and particle-number-conserving Krook model [19]. However, even at large temperatures the enhancement and the inhibition regimes
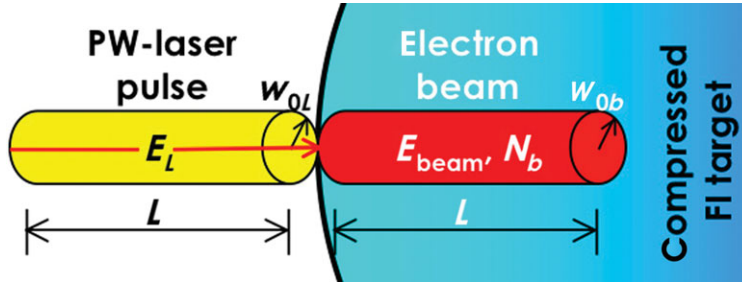
Figure 10. (Colour online) Scheme used to estimate the growth rate of the filamentation instability along a FI pellet profile.

due to collisions as well as the k_{max} position predicted by the theory are qualitatively recovered by simulations.

5. FI scenarios: theoretical predictions

The theoretical model described in Sec. 2 provides us a means to estimate whether the filamentation instability can significantly occur along the compressed FI target by using typical FI parameters. Let us imagine a cylinder-like PW-laser pulse hitting the compressed FI fuel pellet and generating a cylinder-like MeV-electron beam, as sketched in Fig. 10. By knowing the energy E_L and the duration τ_L of the laser pulse, it is possible to calculate the laser energy going into the electrons of the fuel target corresponding to the electron beam energy, as well as the power of the laser pulse. The engineering formulas for the laser pulse power P_L and for the electron beam energy E_{beam} are

$$P_L(\text{PW}) = \left(\frac{E_L}{1\,\text{kJ}}\right)\left(\frac{\tau_L}{1\,\text{ps}}\right)^{-1}; \qquad E_{beam}(\text{kJ}) = \left(\frac{\eta}{100\,\%}\right)\left(\frac{E_L}{1\,\text{kJ}}\right), \qquad (15)$$

where η is the laser-to-electron transfer efficiency. From the mean kinetic energy of the beam electrons E_b, the laser spot radius w_{0L} and considering an electron beam length equal to the laser pulse length $L = \tau_L c$ and a beam radius w_{0b} of the same size as that of the laser spot, the density of the beam electrons is given by the following engineering formula:

$$n_b(\text{cm}^{-3}) \simeq 6.636 \times 10^{24} \left(\frac{E_{beam}}{1\,\text{kJ}}\right)\left(\frac{E_b}{1\,\text{MeV}}\right)^{-1}\left(\frac{w_{0b}}{1\,\mu\text{m}}\right)^{-2}\left(\frac{\tau_L}{1\,\text{ps}}\right)^{-1}. \qquad (16)$$

Considering the beam electron proper fluid velocity $u_b = \gamma_b\beta_b \approx (1 - \beta_b^2)^{-1/2}\beta_b$, estimating the total current carried by the electron beam is now straightforward:

$$I_b(\text{MA}) \simeq 1.509 \times 10^{-3}\,\beta_b\left(\frac{n_b}{10^{19}\,\text{cm}^{-3}}\right)\left(\frac{w_{0b}}{1\,\mu\text{m}}\right)^2. \qquad (17)$$

The electron beam is generated at the edge of the FI target, where, for a laser wavelength λ_L, the corresponding critical density (i.e. when $\omega_L = \omega_{pe}$) is

$$n_c = \frac{\pi m_e c^2}{e^2 \lambda_L^2}; \quad n_c(\text{cm}^{-3}) \simeq 1.115 \times 10^{21}\left(\frac{\lambda_L}{1\,\mu\text{m}}\right)^{-2}. \qquad (18)$$

Table 1. Typical Parameters Along a FI Pellet Profile at the Peak of Compression According to a Possible HiPER Scenario with a Gold Cone Insertion [31]

n [cm^{-3}]	r [μm]	v_{ei} [ω_{pe}]	α	$T_{\perp e}$ [eV]
10^{22}	240	0.0001	0.26	1 000
10^{23}	70	0.020	0.026	700
10^{24}	37	0.33	0.0026	150

The ratio between the beam and plasma electron densities (called contrast ratio) at the edge of the FI target is finally

$$\alpha = \frac{n_b}{n_c}. \tag{19}$$

For the sake of simplicity, we do not consider any relativistic correction due to nonlinear phenomena showing up with high-intensity lasers, such as relativistic-induced trasparency [27] and hole boring [28]. As both of these effects lead to a laser pulse penetration into overdense plasmas, the maximum plasma electron frequency allowing for laser propagation will be larger than that predicted by the linear theory; the critical density at the edge of the FI target will be smaller than the density calculated with (18), thus guaranteeing a larger contrast ratio and a consequent larger growth rate of the filamentation instability. Therefore, not considering any relativistic effects related with high-intensity lasers represents a conservative case in which theoretical predictions of the growth rate of the filamentation instability are underestimated.

The proposed European high-power laser facility HiPER [29] is expected to have an ignitor laser beam characterized by an energy $E_L = 80$ kJ, a pulse duration $\tau_L = 10$ ps, a wavelength $\lambda = 1$ μm and a spot size $w_{0L} = 40$ μm [30]. Furthermore, experimental and numerical studies have suggested for HiPER a laser-to-beam electron energy transfer efficiency $\eta \approx 25$ % and the use of a gold cone [2] whose tip is inserted inside the fuel pellet to reduce the distance the beam electrons have to cover to deposit their energy into the core. By plugging this set of parameters in (15), (16), (17) and (18) and considering $w_{0b} = w_{0L}$, $u_b = 5$ and $E_b = 4$ MeV, one obtains a laser pulse power $P_L = 8$ PW, an electron beam energy $E_{\text{beam}} = 20$ kJ, a beam electron density $n_b = 2.592 \times 10^{21}$ cm^{-3} and a beam electron current $I_b = 613.7$ MA, with the critical density $n_c = 1.115 \times 10^{21}$ cm^{-3}. Assuming a distance between the cone tip and the center of the pellet $r = 240$ μm, which, according to Table 1, corresponds to a background plasma density $n = 10^{22}$ cm^{-3}, the contrast ratio at the cone tip is $\alpha = 0.26$. The plasma electron–ion collision frequency is calculated with (13).

Figure 11 shows the growth rate of the filamentation instability as a function of wavenumber for $T_{\perp b} = 100$ keV. Even though the largest growth rate corresponds to the almost collisionless plasma at the tip of the cone, collisions lead to important unstable modes deep inside the FI pellet, with Γ_{max} comparable with the outer growth rate. Due to the high collisionality, the Γ_{max} for a background plasma density $n = 10^{24}$ cm^{-3} is even larger than the maximum growth rate at $n = 10^{23}$ cm^{-3}, making the occurrence of the filamentation instability closer to the core and very likely the consequent enhancement of energy deposition.
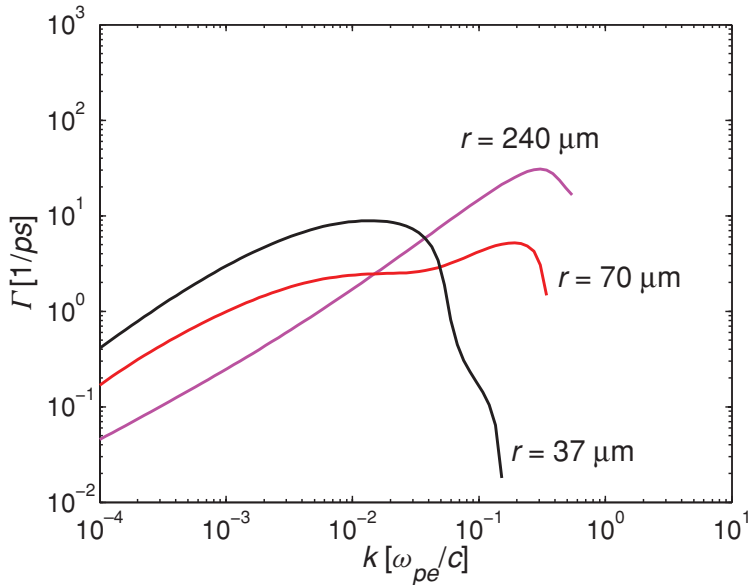
Figure 11. (Colour online) HiPER scenario with a gold cone insertion at 240 μm from the pellet center: growth rate of the filamentation instability as a function of wavenumber for $T_{\perp b} = 100$ keV. r represents the distance from the center of the pellet, where $r = 0$.

6. Conclusions

The collisionless–collisional transition effects on the filamentation instability have been investigated both theoretically and numerically in the context of FI. A theoretical model using relativistic kinetic theory to analyze the linear stage of the filamentation instability with the inclusion of collisions through the particle-number-conserving Krook operator has been presented in detail. By comparing the growth rate of the instability in collisionless and collisional scenarios, two main effects are predicted. As the collision frequency increases, the wavenumber k_{max}, corresponding to the maximum value of the growth rate, shifts toward smaller ks, i.e. larger wavelengths: collisions lead to a preferential formation of larger filaments than those in collisionless cases. The inclusion of collisions can lead to either an inhibition or an enhancement of the filamentation instability, depending on the chosen scenario. In the case of enhancement, thermal effects reduce the instability, but they cannot shut it down even for temperatures at which collisionless unstable modes are cancelled out: collisions guarantee the occurrence of the instability regardless of the transverse temperature.

In order to test the collisional effects predicted by the theory, results of 2D PIC simulations with binary collisions have been presented, with beam and return current plasma electrons moving in counter-propagation, in a neutralizing background of moving ions. The comparison of collisionless and collisional scenarios of the temporal evolution of the beam electron density during the linear stage of the filamentation instability shows a preferential formations of larger filaments than those in collisionless simulations, correctly recovering the k_{max} shifting toward larger wavelengths due to collisions predicted by the theory. The temporal evolution

of the momentum along the propagation direction against the momentum along the transverse direction for collisional simulations shows a strong plasma electron isotropization and a beam electron slowdown. From the collisionless fluid theory it has been shown that, depending on the initial γ_b, in strongly collisional scenarios collisions can lead to either an inhibition or an enhancement of the filamentation instability due to the beam electron slowdown. This physical picture, which qualitatively confirms the theoretical predictions concerning the inhibition–enhancement regimes due to collisions, has been tested with high-resolution 1D PIC simulations by calculating the numerical growth rate of the filamentation instability. The agreement between the theoretical and numerical growth rates of the filamentation instability is very good for both collisionless and collisional scenarios, recovering both the k_{max} shifting toward larger wavelengths and the inhibition–enhancement regimes due to collisions predicted by the theory. For high transverse temperatures, the quantitative agreement in the collisional scenario is not as good as in the low transverse temperature scenarios, thus suggesting the unreliability of the non-energy-conserving Krook operator used in the theory. However, the inhibition–enhancement regimes as well as the k_{max} position predicted by the theory are qualitatively recovered by the simulations even in these scenarios.

Once numerically tested, the theoretical model has been applied to a possible HiPER scenario: the analysis of the growth rate of the filamentation instability along a FI pellet profile reveals that the growth rate is strongly reduced by the transverse temperature and by the small density ratio α as one moves toward the center. However, there can be scenarios in which collisions sustain the instability deeply inside the target: the filamentation instability can then contribute as a mechanism to deposit the beam electron energy in the center of the FI pellet.

References

[1] Tabak, M. et al. 1994 *Phys. Plasmas* **1**, 1626.

[2] Kodama, R. et al. 2002 *Nature* **412**, 798; (2002) **418**, 933.

[3] Weibel, E. S. 1959 *Phys. Rev. Lett.* **2**, 83.

[4] Medvedev, M. V. and Loeb, A. 1999 *Astrophys. J.* **526**, 697; Silva, L. O., Fonseca, R. A., Tonge, J. W., Dawson, J. M., Mori, W. B. and Medvedev, M. V. 2003 *ibid.* **596**, L121; Frederiksen, J. T., Hededal, C. B., Haugbølle, T. and Nordlund, Å. 2004 *ibid.* **608**, L13; Medvedev, M. V., Fiore, M., Fonseca, R. A., Silva, L. O. and Mori, W. B. 2005 *ibid.* **618**, L75.

[5] Ren, C., Tzoufras, M., Tsung, F. S., Mori, W. B., Amorini, S., Fonseca, R. A., Silva, L. O., Adam, J. C. and Heron, A. 2004 *Phys. Rev. Lett.* **93**, 185004.

[6] Yang, T.-Y. B., Arons, J. and Langdon, A. B. 2004 *Phys. Plasmas* **1**, 3059.

[7] Wallace, J. M., Brackbill, J. U., Cranfill, C. W., Forslund, D. W. and Mason, R. J. 1987 *Phys. Fluids* **30**, 1085.

[8] Molvig, K. 1975 *Phys. Rev. Lett.* **35**, 1504.

[9] Honda, M. 2004 *Phys. Rev. E* **69**, 016401.

[10] Deutsch, C., Bret, A., Firpo, M.-C. and Fromy, P. 2005 *Phys. Rev. E* **72**, 026402; Gremillet, L., Bonnaud, G. and Aminaroff, F. 2002 *Phys. Plasmas* **9**, 941; Epperlein, E. M. 1985 *Plasma Phys. Contr. F.* **27**, 1027.

[11] Hao, B., Sheng, Z.-M. and Zhang, J. 2008 *Phys. Plasmas* **15**, 082112.

[12] Hao, B., Sheng, Z.-M., Ren, C. and Zhang, J. 2009 *Phys. Rev. E* **79**, 046409.

[13] Bhatnagar, P. L., Gross, E. P. and Krook, M. 1954 *Phys. Rev.* **94**, 511.

[14] Tzoufras, M., Ren, C., Tsung, F. S., Tonge, J. W., Mori, W. B., Fiore, M., Fonseca, R. A. and Silva, L. O. 2006 *Phys. Rev. Lett.* **96**, 105002.

[15] Fiore, M., Silva, L. O., Ren, C., Tzoufras, M. A. and Mori, W. B. 2006 *Mon. Not. R. Astron. Soc.* **372**, 1851.

[16] Davies, J. R., Bell, A. R., Haines, M. G. and Guérin, S. M. 1997 *Phys. Rev. E* **56**, 7193.

[17] Fiore, M. 2008 Ph.D. thesis, IST.

[18] Delcroix, J.-L. and Bers, A. 1994 In: *Physique des Plasmas*, Vol. 2 (InterÉditions/CNRS Éditions). Paris, p. 182.

[19] Opher, M., Morales, G. J. and Leboeuf, J. N. 2002 *Phys. Rev. E* **66**, 016407.

[20] Cottrill, L. A., Langdon, A. B., Lasinski, B. F., Lund, S. M., Molvig, K., Tabak, M., Town, R. P. J. and Williams, E. A. 2008 *Phys. Plasmas* **15**, 082108.

[21] Silva, L. O., Fonseca, R. A., Tonge, J. W., Mori, W. B. and Dawson, J. M. 2002 *Phys. Plasmas* **9**, 2458.

[22] Sentoku, Y., Mima, K., Kojima, S. and Ruhl, H. 2000 *Phys. Plasmas* **7**, 689.

[23] Fonseca, R. A., Silva, L. O., Hemker, R. G., Tsung, F. S., Decyk, V. K., Lu, W., Ren, C., Mori, W. B., Deng, S., Lee, S., Katsouleas, T. and Adams, J. C. 2002 *Lecture Notes Comput. Sci.* **2331**, 342.

[24] Peano, F., Marti, M., Silva, L. O. and Coppa, G. 2009 *Phys. Rev. E* **79**, 025701(R).

[25] Takizuka, T. and Abe, H. 1977 *J. Comput. Phys.* **25**, 205.

[26] Hockney, R. W. and Eastwood, J. W. 1988 *Computer Simulation Using Particles*. Bristol: Institute of Physics Publishing, p. 318.

[27] Kaw, P. and Dawson, J. 1970 *Phys. Fluids* **13**, 472.

[28] Wilks, S. C., Kruer, W. L., Tabak, M. and Langdon, A. B. 1992 *Phys. Rev. Lett.* **69**, 1383.

[29] Dunne, M. 2006 *Nature Phys.* **2**, 2.

[30] The HiPER project – Technical Background and Conceptual Design Report, from http://www.hiper-laser.org/docs/tdr/HiPERTDR2.pdf.

[31] Ren, C. and Betti, R. Data courtesy, 2006.